Pang *et al. Energy Mater* 2023;3:300012
**DOI:** 10.20517/energymater.2022.81

**Energy Materials**

**Article**

**Open Access**

Check for updates

# Revealing energy storage mechanism of $CsPbBr_3$ perovskite for ultra-stable symmetric supercapacitors

**Le Pang, Minh Tam Hoang, Anthony P. O'Mullane, Hongxia Wang***

School of Chemistry and Physics, Faculty of Science, Queensland University of Technology (QUT), Brisbane, QLD 4001, Australia.

***Correspondence to:** Prof. Hongxia Wang, School of Chemistry and Physics, Faculty of Science, Queensland University of Technology (QUT), Brisbane, QLD 4001, Australia. E-mail: hx.wang@qut.edu.au

**How to cite this article:** Pang L, Hoang MT, O'Mullane AP, Wang H. Revealing energy storage mechanism of $CsPbBr_3$ perovskite for ultra-stable symmetric supercapacitors. *Energy Mater* 2023;3:300012. https://dx.doi.org/10.20517/energymater.2022.81

**Received:** 25 Nov 2022 **First Decision:** 15 Dec 2022 **Revised:** 29 Jan 2023 **Accepted:** 20 Feb 2023 **Published:** 3 Apr 2023

**Academic Editors:** Wei Tang, Jiazhao Wang **Copy Editor:** Fangling Lan **Production Editor:** Fangling Lan

## Abstract

Inorganic metal halide perovskites such as $CsPbX_3$ (X = I, Br) have been intensively studied in optoelectrical applications such as solar cells and light-emitting diodes due to better thermal and structural stability compared to the organic-inorganic hybrid perovskite counterparts. Limited studies have shown that inorganic perovskites could potentially be promising electrode materials in energy storage devices like supercapacitors. Nevertheless, there is some controversy regarding their electrochemical properties and energy storage mechanism. Furthermore, the stability of the inorganic perovskites in electrochemical energy storage systems is a big concern. In this work, we studied the electrochemical properties of $CsPbBr_3$ electrodes composed of pure $CsPbBr_3$ nanocrystals without any additives to reveal their intrinsic electrochemical characteristics. We carefully selected the electrolyte solution composed of tetrabutylammonium hexafluorophosphate in dichloromethane and the electrode substrate based on FTO glass to ensure they do not cause damage to the perovskite material or introduce side reactions during the charge-discharge process. The results showed that the $CsPbBr_3$ perovskite demonstrates electrical double-layer capacitive behaviour, and the specific capacitance of the electrode can reach 528 mF $g^{-1}$. A symmetrical supercapacitor based on this perovskite demonstrated exceptional cycling stability with a capacitance retention of 90% after 10,000 charge and discharge cycles at a discharge current density of 100 mA $g^{-1}$. The device also exhibited a constant power density of 25.0 mW $kg^{-1}$ with increasing energy density up to 33.3 mWh $kg^{-1}$. Further characterizations have revealed the important role of the large cations and anions of tetrabutylammonium hexafluorophosphate in the electrolyte in stabilizing the perovskite electrode material.

**Keywords:** $CsPbBr_3$ perovskite nanocrystals, energy storage mechanism, supercapacitors, stability, long cycling lifetime

## INTRODUCTION

Metal halide perovskites that adopt the chemical formula of $ABX_3$ (X = I, Br, Cl) where A is a monovalent cation such as $MA^+$, $FA^+$ or $Cs^+$ (MA: methyl ammonium, FA: formamidinium), and B is a divalent cation such as $Pb^{2+}$, $Sn^{2+}$[1] have demonstrated exceptional performance in optoelectronic devices like solar cells, light emitting diodes *etc*.[2] owing to their strong light absorption, tuneable bandgap, unexceptional tolerance to defects and facile film processibility by cost-effective solution processing[3,4]. Exploration of metal halide perovskite materials in energy storage devices was first reported by Xia *et al.*, who demonstrated that $MAPbI_3$ and $MAPbBr_3$ could be used as anode materials in lithium-ion batteries[5]. Kostopoulou *et al.* demonstrated that $CsPbBr_3$ microcubes exhibit good electrochemical performance in a Li-ion battery, with a specific capacity of 549 mAh $g^{-1}$[6]. Paul *et al.* also reported using $CsPbBr_3$ as an active anode material in half- and full-lithium-ion batteries. The fabricated half-cell exhibited a discharge specific capacity of 376 mAh $g^{-1}$ at a current density of 30 mA $g^{-1}$[7]. Liu *et al.* used carbon nanotubes wrapped around $CsPbBr_3$ as the anode of a Li-ion battery, which exhibited a reversible capacity of 644.6 mAh $g^{-1}$ at a current density of 100 mA $g^{-1}$ due to the embedded pseudocapacitive behaviour[8]. Further studies have shown that the reduction of $Pb^{2+}$, generating different forms of LiPb alloys, may be responsible for the observed energy storage behaviour, although there are still many open questions regarding the operational mechanism of perovskite electrodes[8-10].

Supercapacitors, also called electrochemical capacitors, are a type of energy storage device that is complementary to batteries with distinctive advantages such as much faster charge and discharge rates (higher power density)[11], outstanding cycling capability and the ability to operate over a broader temperature range[12-14], However, compared to battery research, the study of perovskite in supercapacitors is very rare. This could be related to the notoriously poor stability of perovskites in aqueous electrolyte solutions that are used in most supercapacitors. Only a few reports on perovskite supercapacitors have been reported so far. For example, Zhou *et al. in situ* grown $MAPbI_3$ (methylammonium lead iodide) on a FTO (fluorine-doped tin oxide) glass substrate by a solution method and demonstrated the potential of $MAPbI_3$ as an electrode material and solid electrolyte[10]. Popoola *et al.* fabricated a symmetric $MAPbI_3$ supercapacitor with an areal capacitance of 21.50 μF/$cm^2$[15]. Pious *et al.* used $(CH_3NH_3)_3Bi_2I_9$, a lead-free hybrid perovskite, as the electrode material of their supercapacitor[16]. Li *et al.* reported a new hybrid bismuth halide perovskite electrode $(CN_2SH_5)_3BiI_6$ for supercapacitor and got a high electrode areal capacitance of 3.32 F/$cm^2$[17]. Besides, there are only two reports on supercapacitors using lead halide perovskites nanocrystal such as $CsPbI_3$ microwires[18] or $CsPbBr_3$ microrods[19]. In both cases, the electrode was composed of a perovskite and other additives including conductive carbon black and polyvinylidene fluoride (PVDF) based binder. The symmetric supercapacitor using cesium lead iodide ($CsPbI_3$) microwires as electrodes in an electrolyte of CsI in a butanol solution showed a very low specific capacitance of only 7.23 mF $cm^{-2}$ at a scan rate of 2 mV $s^{-1}$[18]. The other report demonstrated a very high specific capacitance of 121 F $g^{-1}$ for $CsPbBr_3$ microrods on a nickel foam substrate in aqueous KOH electrolytes[19]. However, Ni metal, which is oxidised to NiOOH, is known to have low potential (0.4 V *vs.* saturated calomel reference electrode) for water splitting in the potential range where the supercapacitor operates[20,21]. It is also known metal halide perovskites are extremely sensitive to their chemical environment, including the polarity of the solvent and the supporting ions in electrolyte[9]. A polar solvent can decompose the perovskite compound, while small cations such as $K^+$ can enter the crystal structure of the perovskite[22]. Therefore, to obtain meaningful and accurate results, it is critical to select an electrolyte that does not cause decomposition of the

perovskite as well as a stable substrate that does not exhibit electrochemical reactions within the operational voltage window of the supercapacitors. The limited studies mentioned above all have certain drawbacks, such as low specific capacitance, poor cycle stability, and absence of mechanism explanation. Our material shows an outstanding performance among the other reported perovskite electrode materials [Supplementary Table 1].

In this work, we investigated the intrinsic electrochemical properties of $CsPbBr_3$ perovskite by using an electrode of pure $CsPbBr_3$ nanocrystals coated on a FTO glass substrate without any additives in an organic electrolyte solution composed of tetrabutylammonium hexafluorophosphate ($TBAPF_6$) in dichloromethane (DCM). We found that this perovskite material showed outstanding stability in this electrolyte and demonstrated the characteristic behaviour of an electrical double-layer capacitor with a nearly ideal rectangular shape in the cyclic voltammetry (CV) plots and a triangle shape in galvanic charge-discharge plots (GCD). Using optimal concentration of $TBAPF_6$ in the electrolyte, the potential window increased from 0.8 V to 1 V, and the specific capacitance of the $CsPbBr_3$ electrode reached 528 mF $g^{-1}$ (264 mF $cm^{-2}$ based on the area of active material) at a current density of 100 mA $g^{-1}$. A symmetrical supercapacitor using the $CsPbBr_3$ perovskite exhibited remarkable capacitance retention of 90% after 10,000 charge and discharge cycles. An energy density and power density of 33.3 mWh $kg^{-1}$ and 25.0 mW $kg^{-1}$, respectively, were obtained at a current density of 100 mA $g^{-1}$. The device is more suitable for electrical components that need small current (μA or mA) and long cycle life, such as signal lights, sensors, watches, signal receivers, controllers, and current buffers[23-25].

## EXPERIMENTAL

### Synthesis of the $CsPbBr_3$ perovskite

$CsPbBr_3$ nanocrystals were synthesized by a hot injection method, as reported by us previously[26-28]. Briefly, a precursor solution composed of 203 mg caesium carbonate ($Cs_2CO_3$), 10 mL 1-octadecene (ODE) (95%, Sigma-Aldrich), and 1.5 mL oleic acid (OA) (90%, Sigma-Aldrich) was heated in a round bottom flask under vacuum at 120 °C for 1 h. The temperature was then increased to 160 °C and the solution was heated for 20 min in a nitrogen atmosphere until the solid was completely dissolved to form a Cs-oleate solution that is kept at 120 °C for further use. 207 mg lead bromide ($PbBr_2$), 15 mL ODE, 1.5 mL oleic acid, and 1.5 mL oleylamine (OAM) were mixed in another round bottom flask to form the main solution. The main solution was firstly heated at 120 °C for 1 h under vacuum, and then at 160 °C in a nitrogen atmosphere for 20 min until the solid dissolved completely. After that, 2 mL of the precursor (Cs-oleate) solution was injected into the main solution at 160 °C, which was immediately transferred to a round bottom flask in an ice bath to decrease the solution temperature to room temperature. The color of the solution turned light yellow, suggesting the formation of $CsPbBr_3$ nanocrystals. 15 mL methyl acetate was added to the solution as an antisolvent to promote precipitation of the $CsPbBr_3$ nanocrystals in the solution. The solution was centrifuged at 12,000 rpm for 10 min. The supernatant was decanted, and the precipitate at the bottom of the centrifuge tube was redispersed in hexane to remove the residual ODE, unreacted reactants, and excessive organic ligand (oleic acid and oleylamine), which can make the $CsPbBr_3$ more stable. 15 mL methyl acetate was added to facilitate the precipitation of $CsPbBr_3$ nanocrystals again. After centrifugation at 8,000 rpm for 5 min, the $CsPbBr_3$ nanocrystals at the bottom of the centrifuge tube were collected and dried under vacuum for 12 h at room temperature to completely remove residual solvent.

### Characterization of $CsPbBr_3$

The morphology and structure of the as-synthesized $CsPbBr_3$ nanocrystal powder was measured with scanning electron microscopy (SEM, JEOL 7001F) and transmission electron microscopy (TEM, JEOL 2100). The composition of the perovskite was measured by energy dispersive X-Ray spectroscopy (EDS). The voltage used in the SEM and EDS measurements were 5 kV and 15 kV, respectively, to avoid damaging

the perovskite material. The optical properties of the $CsPbBr_3$ nanocrystals were measured by a UV-VIS spectrophotometer (CARY 60 Romulus) and photoluminescence (PL) spectrophotometer (Cary Eclipse Argus) by dispersion of the as-synthesized material in hexane. X-ray diffraction (XRD, CuKα) patterns and X-ray photoelectron spectroscopy (XPS) measurements of thin films of $CsPbBr_3$ nanocrystals. The films were made by spin coating a solution containing 0.58 mg of the as-synthesised $CsPbBr_3$ in 10 mL hexane on the surface of a FTO substrate. Inductively coupled plasma mass spectrometry (ICP-MS) was used to quantitatively analyze the composition of the electrolyte solution after the electrochemical cycling test, and the standard deviation and residual standard deviation of the results are shown in Supplementary Table 2.

### Preparation of a $CsPbBr_3$ electrode and a symmetric supercapacitor

A $CsPbBr_3$ electrode was made by spin coating the dispersion of $CsPbBr_3$ nanocrystals in hexane (5.8 mg $CsPbBr_3$ nanocrystals in 10 mL hexane) on a cleaned FTO substrate. The FTO glass substrate was washed with Decon 90 solvent under sonication for 20 min, followed by a mixed solvent of acetone, ethanol, and isopropanol at a ratio of 1:1:1 under sonication for another 20 min. After this, the FTO substrate was treated under UV light in an ozone atmosphere for 30 min to remove organic residuals and increase the surface wettability. The process for spin coating was performed at 1,000 rpm $s^{-1}$ for 10 s with an acceleration rate of 100 rpm $s^{-1}$ with a spin coater (CY-SPC8-HAR, Zhengzhou CY Scientific instrument Co., Ltd). After this, the spinning speed was reduced at a rate of 100 rpm $s^{-1}$ for 10 s. The substrate with the sample was dried in a vacuum oven for 12 h. This process was repeated several times until a uniform film with a thickness of around 700 nm was obtained. The excess $CsPbBr_3$ was wiped off with a cotton swab moistened with DMF, leaving the film with a size of 1.0 × 2.0 $cm^2$ [Supplementary Figure 1]. The mass loading (around 1 mg) of the activated material was determined by weighing the difference between the unmodified FTO and the FTO with the $CsPbBr_3$ film. A symmetric $CsPbBr_3$ supercapacitor was assembled by immersing the two $CsPbBr_3$ electrodes with similar mass loading of activated materials in an electrolyte solution composed of $TBAPF_6$ at different concentrations in DCM. In comparison, we also tested the stability of the perovskite electrode in a 1 M KOH aqueous solution.

### Electrochemical characterization

The electrochemical properties of the $CsPbBr_3$ perovskite material were measured using a three-electrode configuration composed of a $CsPbBr_3$-based working electrode, a saturated calomel reference electrode, and a platinum plate counter electrode. The electrolyte solution was composed of $TBAPF_6$ in DCM solvent with different concentrations. The Cyclic voltammetry (CV) at different scan rates (2 mV $s^{-1}$, 5 mV $s^{-1}$, 10 mV $s^{-1}$, 20 mV $s^{-1}$, and 50 mV $s^{-1}$) in a potential window of 0.0 to 1.0 V, galvanostatic charge-discharge (GCD) at different current densities (40-100 mA $g^{-1}$) and impedance spectrum of the perovskite electrode were recorded with an electrochemical workstation (BioLogic) in air. The electrochemical impedance spectroscopy (EIS) measurements were performed over a frequency range from 0.1 Hz to 10 kHz. The EIS data were fitted by an equivalent circuit via Zview software.

The specific mass capacitance of the electrode was calculated according to the GCD plots specifically by the equation of $C_m = \frac{i \times t}{\Delta V}$ where $i$ is the current density (A $g^{-1}$), $t$ is the discharge time ($s$) and $\Delta V$ is the potential window. The specific areal capacitance is given by $C_a = \frac{C_m \times m}{a}$, where $a$ is the area of the active electrode material in contact with the electrolyte. The specific areal capacitance is based on the area of the electrode active material rather than the normalized areal capacitance. The energy density ($E$) and power density ($P$) were calculated using the expressions $E = \frac{0.5 \times C_m \times V \times 1000}{3600} = \frac{C_m \times V}{7.2}$ and $P = \frac{E \times 3600}{t}$, respectively[13].

## RESULTS AND DISCUSSION

### Effect of electrolyte solution on the stability of $CsPbBr_3$ perovskite

KOH aqueous solution is one of the most used electrolytes in supercapacitors. However, an aqueous electrolyte is not suitable for metal halide perovskite electrode materials because exposure to water can cause material degradation and ultimately destroy the $CsPbBr_3$ structure[29]. To confirm this, we investigated the stability of the $CsPbBr_3$ electrode in a 1 M KOH aqueous solution. We found that the yellow color of the perovskite film quickly disappears after contact with the 1 M KOH electrolyte within 3 s [Supplementary Figure 2A and B]. These results confirm that $CsPbBr_3$ is highly unstable in KOH aqueous solution. We also noticed that in a similar report investigating $CsPbBr_3$ for supercapacitor applications by Thakur *et al.* that Ni foam was used as the substrate for $CsPbBr_3$ materials which reported a specific capacitance of 121 F $g^{-1}$[19]. However, both our experimental results [Supplementary Figure 2C] and previous literature[20,21,30] have shown that Ni metal is not a suitable substrate to assess electrode materials in supercapacitors applications as it can cause water splitting when the voltage is above 0.4 V (*vs.* saturated calomel reference electrode), resulting in inaccuracy or over-estimation of the electrochemical properties of the electrode.

In order to address the moisture instability of $CsPbBr_3$, we used a non-polar organic solution composed of $TBAPF_6$ in low polarity DCM for the electrochemical characterization of $CsPbBr_3$[9]. The large size of both the cation and anion in $TBAPF_6$ benefits the structural stability of $CsPbBr_3$ in solution as they are too bulky to intercalate into the $CsPbBr_3$ crystal structure[9]. In addition, the much lower polarity of DCM (polarity index = 3.1) compared to water (polarity index = 10.2) is expected to hinder the decomposition of the perovskite material. Indeed, we found that the $CsPbBr_3$ film was almost completely intact after 2,000 cycles of electrochemical charge/discharge based on the fluorescence image of the film under a UV light exposure [Supplementary Figure 2D]. These results gave us confidence that $TBAPF_6$ in DCM is a compatible electrolyte for studying the electrochemical properties of $CsPbBr_3$. This is the first time the electrolyte was used in a supercapacitor rather than in other applications.

### Electrochemical performance characterization

The CV behaviour of a $CsPbBr_3$ electrode in a three-electrode configuration in an electrolyte with different concentrations of $TBAPF_6$ in DCM is shown in Figure 1. Figure 1A compares the CV curves of a bare FTO electrode and $CsPbBr_3$ coated FTO. The bare FTO electrode showed negligible capacitance and can be regarded as only a current collector. In contrast, a nearly rectangular-shaped CV curve was obtained with the $CsPbBr_3$ electrode over a wide potential window of 0-0.8 V [*vs.* standard calomel electrode (SCE)] [Figure 1A]. The complete absence of any redox peaks from a faradaic process indicates that the perovskite material operates through an electric double-layer energy storage mechanism that relies on electrolyte ion adsorption/desorption on the electrode surface [Supplementary Figure 3][19,31]. We further investigated the ionic conductivity of the electrolyte as a function of concentration of $TBAPF_6$ in DCM. The results show that the highest conductivity was obtained with 1.5 M $TBAPF_6$ [Figure 1B]. However, such a high concentration of $TBAPF_6$ can result in precipitation of $TBAPF_6$ on the surface of the electrode due to oversaturation of the salt in DCM. The CV curves of the $CsPbBr_3$ electrode in a three-electrode system with different concentrations of $TBAPF_6$ are shown in Figure 1C. The capacitance of the $CsPbBr_3$ electrode increased significantly when the $TBAPF_6$ concentration increased from 0.1 M to 1 M. Beyond this, the capacitance of the $CsPbBr_3$ electrode does not change. The GCD curves [Figure 1D] also confirm the superior properties of the 1 M electrolyte compared to 0.1 M $TBAPF_6$. The 1 M electrolyte exhibits a much longer discharge time at both high (100 mA $g^{-1}$) and low (40 mA $g^{-1}$) current densities, which implies a higher specific capacitance. Therefore, 1 M $TBAPF_6$ electrolyte was used in the following experiments because of its high conductivity and lack of precipitation from solution.

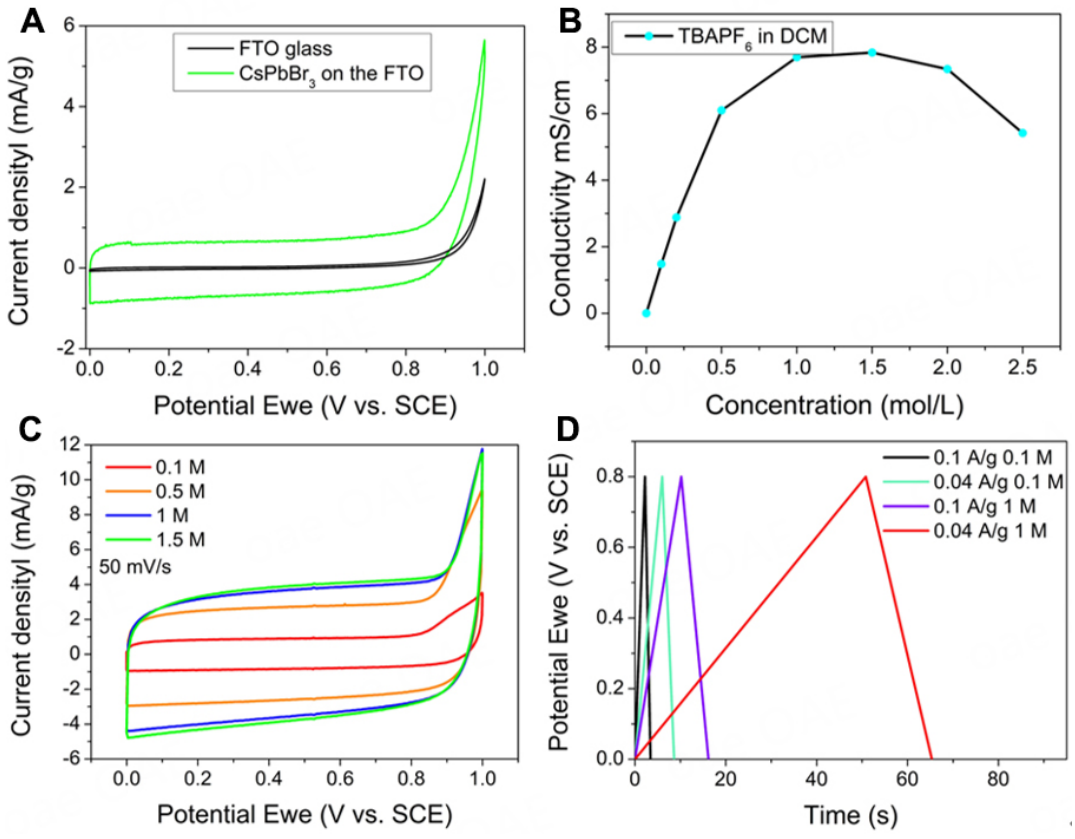


**Figure 1.** (A) Comparison of CV curves of $CsPbBr_3$/FTO electrode and bare FTO in 0.1 M $TBAPF_6$ at a scan rate of 50 mV $s^{-1}$. (B) dependence of ionic conductivities of the electrolyte with different concentrations of $TBAPF_6$ in DCM. (C) CV curves of $CsPbBr_3$ electrode in electrolyte with different concentrations of $TBAPF_6$ in DCM at a scan rate of 50 mV $s^{-1}$. (D) domparison of GCD curves of $CsPbBr_3$ electrode in 0.1 M and 1 M $TBAPF_6$ in DCM at the current density of 0.04 A $g^{-1}$ and 0.1 A $g^{-1}$, respectively.

Nyquist plots of the $CsPbBr_3$ electrode in a three-electrode setup employing 1 M $TBAPF_6$ electrolyte over a frequency range from 0.1 Hz to 100 KHz are shown in Figure 2A and B. A nearly vertical line with a slope of 84° indicates that the $CsPbBr_3$ nanocrystals possess an electric double-layer capacitor (EDLC) capacitive behaviour, which is determined by the diffusion of electrolyte ions between the electrode surface and the electrolyte [Figure 2A][32,33]. Fitting the high-frequency region of the Nyquist plot by using the equivalent circuit shown in the inset of Figure 2A clearly shows the resistance from each part of the system [Figure 2B]. The 1 M $TBAPF_6$ electrolyte had a charge transfer resistance (Rct) of 0.5 Ω and an internal resistance ($R_i$) of 146 Ω. The Warburg impendence is 165 Ω and the CPE (constant phase element) is 1 $Ss^n$ $cm^{-2}$. The series resistance Rs comes from each part of the assembled device and the contacts between the parts, which mainly include the $CsPbBr_3$ electrode, non-dense coating, the organic electrolyte, the FTO glass and the interfacial resistance resulting from the contact between the electrode and electrolyte[34,35]. Figure 2C shows the CV curves of the $CsPbBr_3$ electrode in 1 M $TBAPF_6$ electrolyte over a potential window of 1 V recorded at different scan rates of 2 mV $s^{-1}$, 5 mV $s^{-1}$, 10 mV $s^{-1}$, 20 mV $s^{-1}$, and 50 mV $s^{-1}$, respectively. The near rectangle shape of the CV plots is consistent with the typical shape of EDLC behavior. In addition, there are no redox peaks observed in Figure 2C, indicating that the electrochemical process in the $CsPbBr_3$ nanocrystals does not involve a Faradaic charge transfer process[13,14]. The GCD plots of the $CsPbBr_3$ electrode in 1 M $TBAPF_6$ electrolyte with the current density increasing from 40 to 100 mA $g^{-1}$ over a voltage window of 1 V were also measured [Figure 2D]. With the increasing current density, the shape of the curves remains triangular without a discharge plateau, indicating excellent reversible EDLC behaviour. It is noticed

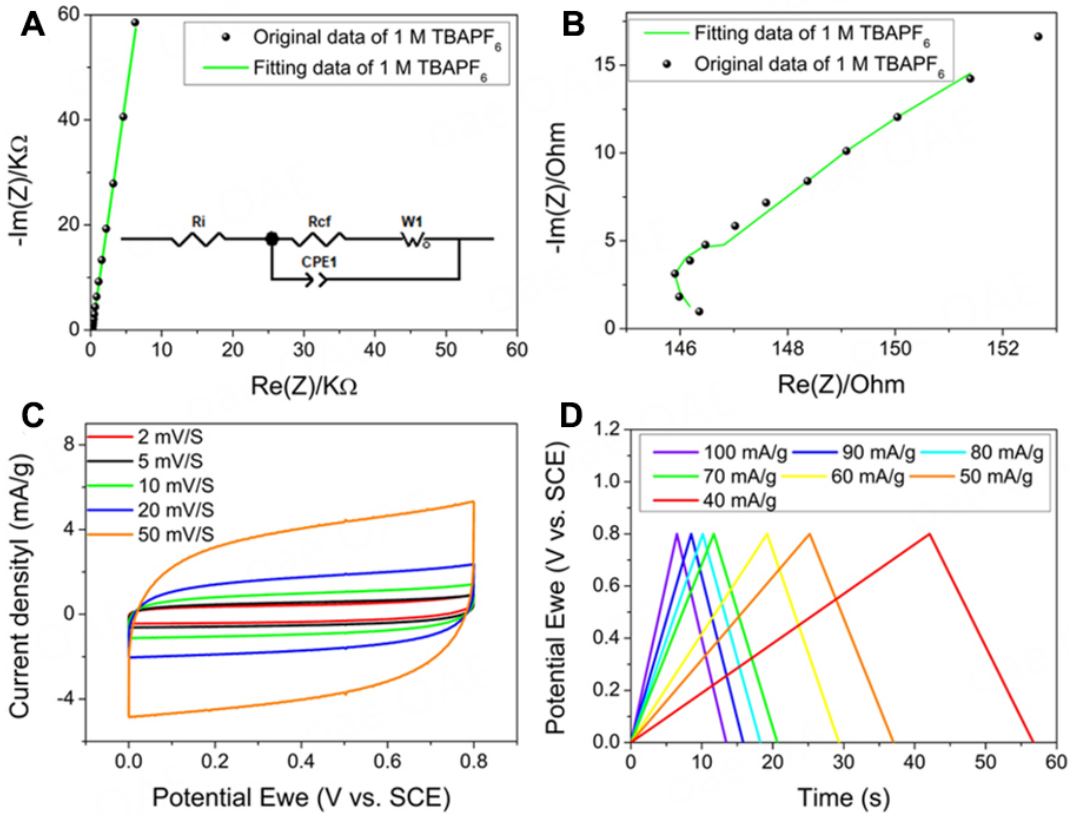


**Figure 2.** Nyquist plot of the $CsPbBr_3$ electrode in 1 M $TBAPF_6$ electrolyte in (A) Low and (B) high-frequency region. The insert is the enlarged curve at the high-frequency region and the equivalent electric circuit. (C) the CV curves of $CsPbBr_3$electrode in 1 M $TBAPF_6$ at different scan rates. (D) the charge and discharge curves of $CsPbBr_3$ electrode in 1 M $TBAPF_6$ at different current densities. All the tests were performed in a three-electrode system in air.

that the coulombic efficiency at low current density (40 mA $g^{-1}$) is poor, which could be caused by the slow ion absorption/desorption and faster degradation of the perovskite[36]. Based on the GCD plots, the mass specific capacitance of the $CsPbBr_3$ electrode was calculated to be 528 mF $g^{-1}$ (264 mF $cm^{-2}$) at a current density of 100 mA $g^{-1}$ [Figure 2D]. These tests were repeated in $N_2$ atmosphere and gave similar results [Supplementary Figure 4].

To further confirm the energy storage mechanism of the perovskite electrode, a relationship based on a power law between the current ($i$) and the scan rate ($v$) was investigated according to $\log i(V) = blogv + loga$[37], where $i$ is the current, $v$ is the scan rate. We extracted the $b$ value by fitting the plot of log $i$ *vs.* log $v$ [Figure 3A]. The value of $b$ is 0.89, which is close to 1, indicating capacitive behaviour. To confirm the contribution of diffusion in the charge storage process, we fitted the plot of current density *vs.* potential with $i(V) = K_1v + K_2v^{1/2}$[37], where $i$ is the current, $V$ is the voltage and $v$ is the scan rate [Figure 3B]. The result shows that 99.33% of the capacitance is due to an EDLC process. Furthermore, measurement of the high-resolution XPS for Cs, Pb and Br on the surface of the perovskite electrode before and after the electrochemical test shows no change in the XPS peaks after 2,000 cycles [Supplementary Figure 5]. This indicates that there is no change in the chemical state of the elements in the perovskite. Jiang *et al.* proved that only small ions like $Li^+$ and $Na^+$ can intercalate into the perovskite structure to form Pb metal which is called an electrochromic phenomenon[38]; however, large ions like $K^+$ and $Cs^+$ exceed the intercalation limit of perovskite[38], and are hence excluded from entering the crystal structure. Therefore, the $TBAPF_6$ electrolyte cannot provide the required conditions to form Pb metal which would degrade the structure.

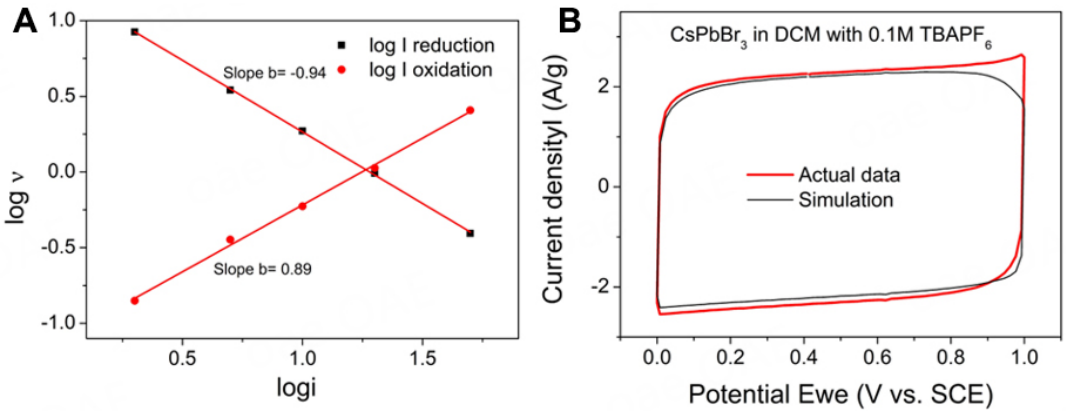


**Figure 3.** (A) Demonstration of the Trasatti method. (B) the simulation calculation of CV curve $CsPbBr_3$ electrode in three-electrode system in 0.1 M $TBAPF_6$ at a scan rate of 50 mV $s^{-1}$ (Dunn method).

Symmetrical supercapacitors (SCs) composed of two identical $CsPbBr_3$ electrodes with similar active material loading were fabricated to assess the energy and power density of the device as well as cycling stability. To demonstrate the importance of the $TBAPF_6$ concentration on the device performance, we compared supercapacitors using 0.1 M and 1 M $TBAPF_6$ in DCM electrolytes. The SC using 0.1 M $TBAPF_6$ is named SS-0.1, while the one using 1 M $TBAPF_6$ in DCM is named SS-1, respectively. The CV curves of SS-1 [Figure 4A] at different scan rates over a potential window of 0-1.0 V are even closer to a rectangle than the CV curves in a three-electrode system, further confirming the EDLC behaviour of the $CsPbBr_3$ nanocrystals[10,13]. The shape of the CV is well maintained at a high scan rate of 50 mV $s^{-1}$, indicating good rate performance. Figure 4B shows the charge and discharge curves of the SS-1 at different current densities over a current density range from 40 to 100 mA $g^{-1}$. It was found that the shape of the curves remained triangular with no noticeable voltage drop upon an increase in the current density. The calculated specific capacitances of SS-1 and SS-0.1 are 119.8 mF $g^{-1}$ (60.88 mF $cm^{-2}$) and 30.5 mF $g^{-1}$ (17.75 mF $cm^{-2}$), respectively, at a current density of 100 mA $g^{-1}$. Figure 4C compares the specific capacitances of SS-0.1 and SS-1 at different current densities, where it is worth noting that the specific capacitance of SS-1 is nearly 4 times higher than SS-0.1. Both devices demonstrate more than 90% capacitance retention with an increase of current density from 40 mA $g^{-1}$ to 100 mA $g^{-1}$, which indicates the excellent rate performance of the perovskite.

Figure 4D shows the cycle stability of SS-0.1 and SS-1. It was found that the specific capacitance of SS-0.1 dropped to 78.86% of its initial value after 2,000 cycles at a current density of 100 mA $g^{-1}$ [Figure 4D]. In contrast, SS-1 showed superior cycle stability with negligible change in the specific capacitance in the first 2,000 cycles. Even after 10,000 cycles, a retention rate of 90.43% was obtained. The energy density and power density of SS-0.1 and SS-1 are shown in Figure 4E, where SS-0.1 and SS-1 show the same power density which increases from 10 mW $kg^{-1}$ to 25 mW $kg^{-1}$ upon an increase in the current density. On the other hand, the energy density of SS-1 is four times higher than that of SS-0.1 at the same applied current density. The small decreases in energy density from 9.4 mWh $kg^{-1}$ to 8.5 mWh $kg^{-1}$ for SS-0.1 and from 35.0 mWh $kg^{-1}$ to 33.3 mWh $kg^{-1}$ for SS-1 were observed with an increase in discharge current density from 40 mA to 100 mA $g^{-1}$. Ragone plots of SS-0.1 and SS-1 in Figure 4F are almost two horizontal lines, and the increase in power density does not weaken the energy density significantly, which is highly desirable for the practical application of this material in a supercapacitor.

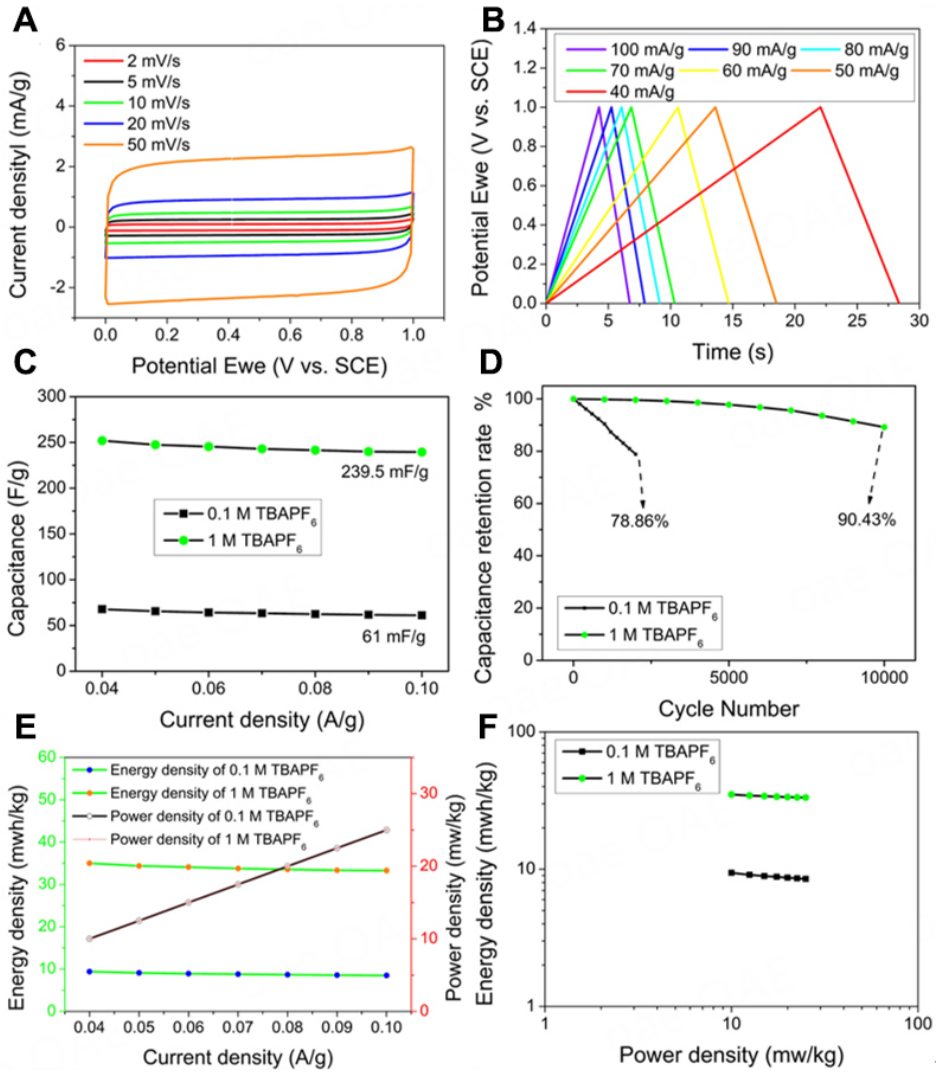


**Figure 4.** (A) The CV curves of SS-1 under different scan rates. (B) the charge and discharge curves SS-1 at different current densities. (C) the specific capacitance of SS-0.1 and SS-1 at different current densities. (D) cycling stability of SS-0.1 and SS-1 after 2,000 and 10,000 cycles at a current density of 100 mA $g^{-1}$. (E) energy density and power density of SS-0.1 and SS-1 at different current densities. (F) relationship between energy density and power density of SS-0.1 and SS-1 (Ragone plot).

### Understanding the cycle stability of the $CsPbBr_3$ electrode

It is clear that the performance of SS-1 is significantly better than SS-0.1, in particular, the cycle stability. Therefore, further research was undertaken to investigate the underlying reasons. After the electrochemical cycling test, characterization of the electrode material in SS-0.1 by EDS shows the formation of larger crystals that are different from the pristine $CsPbBr_3$ crystals on the surface of the $CsPbBr_3$ electrode [Figure 5]. EDS mapping [Figure 5A-F] shows that F and P elements are concentrated on the large crystals while Br and Pb elements are distributed around the large crystals while Cs exists across the whole area. Therefore, this infers that the large crystals are mainly composed of three elements, Cs, P, and F. The EDS line scan also confirms these findings [Supplementary Figure 6A and B]. Supplementary Figure 6B shows the position of the EDS line scan on the large crystal. The concentration of F and P is higher in the region of the large crystals than in their surroundings, while the opposite trend is found for Br and Pb elements. The distribution of Cs is largely uniform. The atomic ratio of P and F is very close to 1:6, proving the existence of the $PF_6^-$ functional group [Supplementary Figure 6C]. Therefore, we suspect that the large crystal is

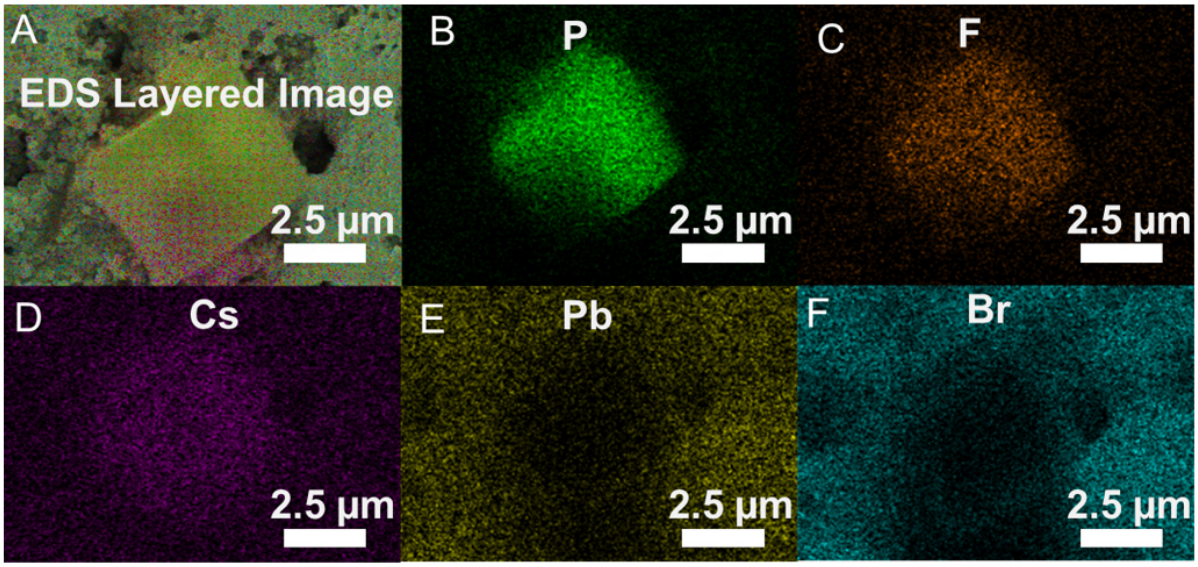


**Figure 5.** EDS mapping of $CsPbBr_3$ electrodes in SS-0.1 after the electrochemical test. (A) the layered image of mapping. Mapping result of different elements (B) F; (C) P; (D) Cs; (E) Br; (F) Pb.

probably a secondary phase, such as $CsPF_6$ formed on the electrode during the electrochemical charge-discharge process. The XRD pattern in Figure 6A confirms that, indeed, besides $CsPbBr_3$, $CsPF_6$ also exists in the electrode. This is consistent with previous reports where $CsPF_6$ was formed in $CsPbBr_3$ in the presence of a $TBAPF_6$ electrolyte[9]. On the other hand, Samu *et al.* postulated that the phase transformation of $CsPbBr_3$ is triggered by the reduction of $Pb^{2+}$ at -1.4 V *vs.* Ag/AgCl reference electrode[9]. However, the reduction potential of $Pb^{2+}$ is -0.13 V *vs.* standard hydrogen electrode, and -0.37 V *vs.* saturated calomel electrode)[39-41], respectively. In addition, our results show that the transformation from $CsPbBr_3$ to $CsPF_6$ can occur even at a low voltage of 0.4 V rather than -1.4 V[6]. Supplementary Figure 7A and B show the SEM of the $CsPbBr_3$ electrode in SS-0.1 after 40 CV cycles at a scan rate of 5 mV $s^{-1}$ over a potential window of 0.4 V. The large cubic crystal should be $CsPF_6$, and the surrounding tiny crystals are $CsPbBr_3$ [Supplementary Figure 7A]. Supplementary Figure 7B shows the distribution of $CsPF_6$ on $CsPbBr_3$ electrode. Therefore, we propose $CsPF_6$ is formed by an ion exchange reaction, as shown in Equation (1).

$$CsPbBr_3 + TBAPF_6 \leftrightarrow TBAPbBr_3 + CsPF_6 \quad (1)$$

The content of each crystal phase in the electrode at different cycling stages was then analyzed quantitatively based on XRD measurements [Figure 6A] using TOPAS software, as shown in Supplementary Table 3. Before the test, $CsPbBr_3$ electrodes contain 89% cubic $CsPbBr_3$ and 11% orthorhombic $CsPbBr_3$. Upon electrochemical cycling, the amount of $CsPF_6$ in the perovskite electrode of SS-0.1 increased with the increase of cycle numbers and reached 24.48% after 2,000 cycles of charge/discharge. In contrast, the contents of $CsPF_6$ in the $CsPbBr_3$ electrode of SS-1 is only 4.01% even after 10,000 cycles, which is much lower than the amount of $CsPF_6$ in SS-0.1. Therefore, a high concentration of $TBAPF_6$ can effectively hinder the dissolution of the perovskite in the electrolyte, preventing the formation of $CsPF_6$. To confirm this hypothesis, we measured the content of Cs and Pb in the electrolyte of the SS-0.1 and SS-1 devices after 2,000 cycles by ICP-MS. The results [Figure 6B] show that the concentrations of Cs and Pb ions in the electrolyte of SS-0.1 are 4.4 ppm (mg $L^{-1}$) and 8.7 ppm (mg $L^{-1}$), respectively, while their concentrations in the electrolyte of SS-1 are significantly lower with values of 0.083 and 0.91 ppm (mg $L^{-1}$), respectively. This confirms the importance of having a high concentration of $TBAPF_6$ in the electrolyte to stabilize the

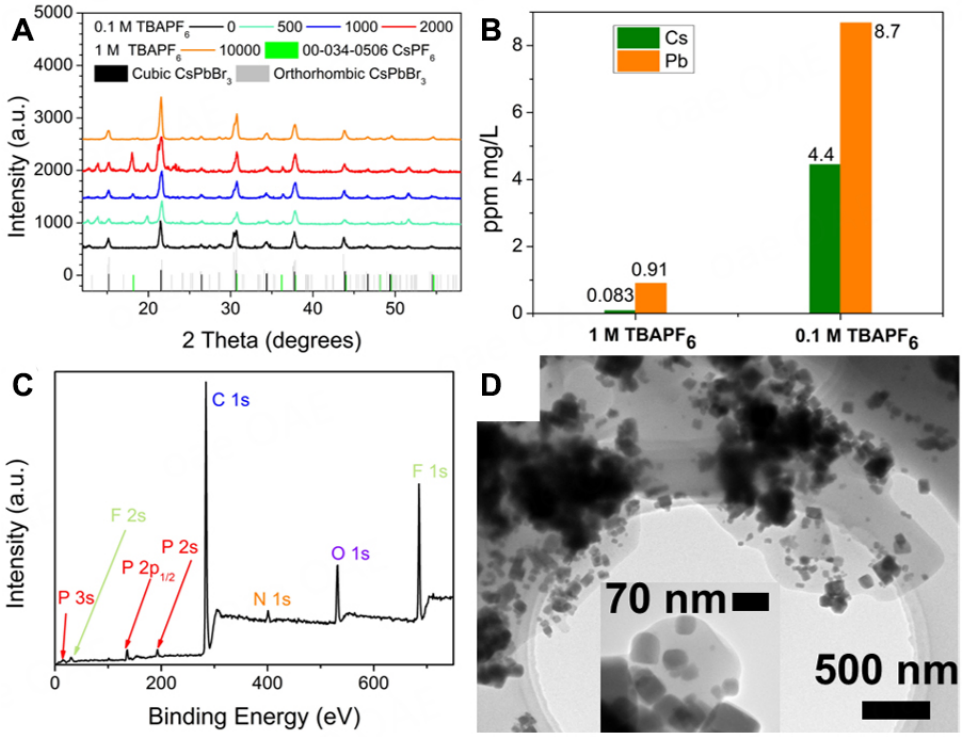


**Figure 6.** (A) The XRD scan of SS-0.1 and SS-1 after the cycles of charge/discharge. (B) the ICP-MS results of SS-0.1 and SS-1 after 2,000 cycles of charge/discharge. (C) XPS of $CsPbBr_3$ electrode in SS-1 after 2,000 cycles of charge and discharge without etching process. (D) TEM of $TBAPF_6$ covered $CsPbBr_3$ crystal obtained from $CsPbBr_3$ electrode after 2,000 cycles of charge and discharge.

perovskite electrode materials. This could be related to suppressed decomposition or reorganization of $CsPbBr_3$ surrounded by a high concentration of large electrolyte ions, because of the formation of the nano-scaled film on the surface of the $CsPbBr_3$ electrode, thereby increasing the overall cycling stability of the supercapacitor. The XPS wide scan without etching for the $CsPbBr_3$ electrode in SS-1 after 2,000 cycles of charge and discharge in Figure 6C indicates that the elements present in the film on the $CsPbBr_3$ electrode surface only include C, N, O, P, and F rather than Cs, Pb, and Br. For further investigation, the components on the electrode in SS-1 were redispersed in hexane for TEM measurements. TEM images in Figure 6D visually show that the $CsPbBr_3$ nanocrystals still keep a cubic shape and were wrapped in an amorphous substance, which could be $TBAPF_6$. Further investigations carried out by FTIR [Supplementary Figure 8] proved the existence of the $PF_6^-$ functional group on the electrode. The absence of $TBAPF_6$'s peaks in the XRD pattern [Figure 6A] also indicates that the $TBAPF_6$ is amorphous, which is consistent with the TEM results. Therefore, the dramatically increased stability resulted from the coverage of amorphous $TBAPF_6$ on the $CsPbBr_3$ electrode, which only happens at high concentrations. Additionally, although the $TBAPF_6$ layer (solid electrolyte interphase) covered on the surface of the electrode prevents the perovskite from decomposing, it also reduces the coulombic efficiency because it hinders the ion transfer from electrolyte to the surface of $CsPbBr_3$ for adsorption. Moreover, side reactions such as the formation of $CsPF_6$ could reduce the coulombic efficiency to some extent, especially at low current densities. Supplementary Figure 9 shows the cycle stability of SS-1 at a current density of 40 mA/g and Cs ions concentration in the electrolyte after 2,000 cycles. The retention rate of SS-1 at a current density of 40 mA/g after 2,000 cycles is 89.77% [Supplementary Figure 9A]. We can see that the concentration of Cs and Pb under low current density is much higher than the one under high current density [Supplementary Figure 9B].

Specifically, it is known that the chemical bonding strength between the $Cs^+$cation in the perovskite crystal structure with the $[PbBr_x]^-$ the framework is weak, and the energy barrier for migration of $Cs^+$ in the perovskite crystal structure is 0.3-0.7 eV[42-44]. Experimental evidence has shown that $Cs^+$ can drift away from the perovskite crystal structure under certain electrical fields which are high enough to overcome the energy barrier for $Cs^+$ migration. Under low current density, it takes a longer time for the electrode to reach the maximum voltage compared to the situation under higher current density. Specifically, according to the GCD plots, it takes 45 s for the charging plot to reach the maximum at 40 mA/g, whereas the charging time is much shorter (55 s) under 100 mA/g. The much higher content of $Cs^+$ ions in the electrolyte at 40 mA/g than that at 100 mA/g indicates that $Cs^+$ ions have sufficient time to drift out of the perovskite crystal structure when the current density is low (40 mA/g), which eventually leads to the collapse of the perovskite structure because $Cs^+$ plays a role in stabilizing the crystalline lattice in perovskite[45-47]. The high concentration of $Cs^+$ will also improve the formation of $CsPF_6$ (side reaction). In comparison, the faster charging/discharge at the larger current density means $Cs^+$ ions might not have sufficient time to leave the perovskite.

## CONCLUSIONS

In conclusion, we synthesized $CsPbBr_3$ nanocrystals by a hot injection method and investigated the electrochemical properties of the materials in a three-electrode system and symmetrical supercapacitor. Our research has shown that 1 M $TBAPF_6$ in DCM electrolyte is the most suitable electrolyte for ensuring the stability of $CsPbBr_3$. CV, GCD, and XPS experiments demonstrated the electric double-layer energy storage mechanism of $CsPbBr_3$. The specific capacitance of $CsPbBr_3$ can reach as high as 528 mF $g^{-1}$, while the specific capacitance of the symmetrical supercapacitor is 119.8 mF $g^{-1}$ at a current density of 100 mA $g^{-1}$ with a potential window of 0-1.0 V. A high retention rate of 90.43% was achieved after 10,000 cycles of charging and discharging at a current density of 100 mA $g^{-1}$. The power density and energy density of the $CsPbBr_3$ symmetric supercapacitor are 25 mWh $kg^{-1}$ and 33.3 mW $kg^{-1}$, respectively, at a current density of 100 mA $g^{-1}$. Our research indicates the potential of $CsPbBr_3$ as an electrode material in supercapacitors and this work lays the foundation for future targeted modification of the performance of supercapacitor electrodes using perovskite materials as electrodes.

## DECLARATIONS

### Acknowledgments

We thank Dr. Osama Yousef Ali Ghidan (Sam) for the ICPMS measurement.

### Authors' contributions

Conception and the design of the study: Wang H, Pang L
Methodology, experiment, data acquisition, data analysis, data interpretation and writing: Pang L
Technical and material support: Hoang MT
Chemicals and instrument support: O'Mullane AP

### Availability of data and materials

Not applicable.

### Financial support and sponsorship

This work was supported by the Australian Research Council (ARC) Discovery Project (DP210102580, DP190102252), ARC Linkage Project (LP210100217) Strategic Research.

### Conflicts of interest

All authors declared that there are no conflicts of interest.

### Ethical approval and consent to participate

Not applicable.

### Consent for publication

Not applicable.

### Copyright



## REFERENCES


1. Kumar R, Bag M. Hybrid halide perovskite-based electrochemical supercapacitors: recent progress and perspective. *Energy Technol* 2022;10:2100889. DOI
2. Narayanan S, Parikh N, Tavakoli MM, et al. Metal halide perovskites for energy storage applications. *Eur J Inorg Chem* 2021;2021:1201-12. DOI
3. Wang R, Huang T, Xue J, Tong J, Zhu K, Yang Y. Prospects for metal halide perovskite-based tandem solar cells. *Nat Photon* 2021;15:411-25. DOI
4. Kostopoulou A, Kymakis E, Stratakis E. Perovskite nanostructures for photovoltaic and energy storage devices. *J Mater Chem A* 2018;6:9765-98. DOI
5. Xia HR, Sun WT, Peng LM. Hydrothermal synthesis of organometal halide perovskites for Li-ion batteries. *Chem Commun* 2015;51:13787-90. DOI PubMed
6. Kostopoulou A, Vernardou D, Makri D, Brintakis K, Savva K, Stratakis E. Highly stable metal halide perovskite microcube anodes for lithium-air batteries. *J Power Sources* 2020;3:100015. DOI
7. Paul T, Maiti S, Chatterjee BK, et al. Electrochemical performance of 3D network $CsPbBr_3$ perovskite anodes for Li-ion batteries: experimental venture with theoretical expedition. *J Phys Chem C* 2021;125:16892-902. DOI
8. Liu S, Zhang K, Tan L, Qi S, Liu G, Chen J, et al. All-inorganic halide perovskite $CsPbBr_3$@CNTs composite enabling superior lithium storage performance with pseudocapacitive contribution. *Electrochim Acta* 2021;367:137352. DOI
9. Samu GF, Scheidt RA, Kamat PV, Janáky C. Electrochemistry and spectroelectrochemistry of lead halide perovskite films: materials science aspects and boundary conditions. *Chem Mater* 2018;30:561-9. DOI PubMed PMC
10. Zhou S, Li L, Yu H, Chen J, Wong C, Zhao N. Thin film electrochemical capacitors based on organolead triiodide perovskite. *Adv Electron Mater* 2016;2:1600114. DOI
11. Wang T, Lei J, Wang Y, et al. Approaches to enhancing electrical conductivity of pristine metal-organic frameworks for supercapacitor applications. *Small* 2022;18:2203307. DOI PubMed
12. Zhu Y, Murali S, Stoller MD, et al. Carbon-based supercapacitors produced by activation of graphene. *Science* 2011;332:1537-41. DOI PubMed
13. Wang T, Chen HC, Yu F, Zhao XS, Wang H. Boosting the cycling stability of transition metal compounds-based supercapacitors. *Energy Stor Mater* 2019;16:545-73. DOI
14. Choudhary N, Li C, Moore J, et al. Supercapacitors: asymmetric supercapacitor electrodes and devices. *Adv Mater* 2017;29:1605336. DOI
15. Popoola I, Gondal M, Oloore L, Popoola A, AlGhamdi J. Fabrication of organometallic halide perovskite electrochemical supercapacitors utilizing quasi-solid-state electrolytes for energy storage devices. *Electrochim Acta* 2020;332:135536. DOI
16. Pious JK, Katre A, Muthu C, Chakraborty S, Krishna S, Vijayakumar C. Zero-dimensional lead-free hybrid perovskite-like material with a quantum-well structure. *Chem Mater* 2019;31:1941-5. DOI
17. Li T, Mallows J, Adams K, Nichol GS, Thijssen JH, Robertson N. Thiourea bismuth iodide: crystal structure, characterization and high performance as an electrode material for supercapacitors. *Batteries Supercaps* 2019;2:568-75. DOI
18. Maji P, Ray A, Sadhukhan P, Roy A, Das S. Fabrication of symmetric supercapacitor using cesium lead iodide ($CsPbI_3$) microwire. *Mater Lett* 2018;227:268-71. DOI
19. Thakur S, Paul T, Maiti S, Chattopadhyay KK. All-inorganic $CsPbBr_3$ perovskite as potential electrode material for symmetric supercapacitor. *Solid State Sci* 2021;122:106769. DOI
20. Chen L, Dong X, Wang Y, Xia Y. Separating hydrogen and oxygen evolution in alkaline water electrolysis using nickel hydroxide. *Nat Commun* 2016;7:11741. DOI PubMed PMC
21. Li J, Wang S, Chang J, Feng L. A review of Ni based powder catalyst for urea oxidation in assisting water splitting reaction. *Adv Powder Technol* 2022;1:100030. DOI
22. Yao D, Zhang C, Pham ND, et al. Hindered formation of photoinactive δ-$FAPbI_3$ phase and hysteresis-free mixed-cation planar

heterojunction perovskite solar cells with enhanced efficiency via potassium incorporation. *J Phys Chem Lett* 2018;9:2113-20. DOI PubMed

23. Wang Y, Zhou W, Kang Q, et al. Patterning islandlike $MnO_2$ arrays by breath-figure templates for flexible transparent supercapacitors. *ACS Appl Mater Interfaces* 2018;10:27001-8. DOI PubMed
24. Chu D, Li F, Song X, et al. A novel dual-tasking hollow cube $NiFe_2O_4$-NiCo-LDH@rGO hierarchical material for high preformance supercapacitor and glucose sensor. *J Colloid Interface Sci* 2020;568:130-8. DOI PubMed
25. Zhang L, Hu X, Wang Z, Sun F, Dorrell DG. A review of supercapacitor modeling, estimation, and applications: a control/management perspective. *Renew Sustain Energy Rev* 2018;81:1868-78. DOI
26. Hoang MT, Pannu AS, Tang C, et al. Potassium doping to enhance green photoemission of light-emitting diodes based on $CsPbBr_3$ perovskite nanocrystals. *Adv Opt Mater* 2020;8:2000742. DOI
27. Hoang MT, Pannu AS, Yang Y, et al. Surface treatment of inorganic $CsPbI_3$ nanocrystals with guanidinium iodide for efficient perovskite light-emitting diodes with high brightness. *Nano-Micro Lett* 2022;14:69. DOI PubMed PMC
28. Kostopoulou A, Brintakis K, Nasikas NK, Stratakis E. Perovskite nanocrystals for energy conversion and storage. *Nanophotonics* 2019;8:1607-40. DOI
29. Hsieh YT, Lin YF, Liu WR. Enhancing the water resistance and stability of $CsPbBr_3$ perovskite quantum dots for light-emitting-diode applications through encapsulation in waterproof polymethylsilsesquioxane aerogels. *ACS Appl Mater Interfaces* 2020;12:58049-59. DOI PubMed
30. Zhu Y, Cao C, Tao S, Chu W, Wu Z, Li Y. Ultrathin nickel hydroxide and oxide nanosheets: synthesis, characterizations and excellent supercapacitor performances. *Sci Rep* 2014;4:5787. DOI PubMed PMC
31. Barbieri O, Hahn M, Herzog A, Kötz R. Capacitance limits of high surface area activated carbons for double layer capacitors. *Carbon* 2005;43:1303-10. DOI
32. Mohanadas D, Mohd Abdah MAA, Azman NHN, Ravoof TBSA, Sulaiman Y. Facile synthesis of PEDOT-rGO/HKUST-1 for high performance symmetrical supercapacitor device. *Sci Rep* 2021;11:11747. DOI PubMed PMC
33. Lin T, Chen IW, Liu F, et al. Nitrogen-doped mesoporous carbon of extraordinary capacitance for electrochemical energy storage. *Science* 2015;350:1508-13. DOI PubMed
34. Yen MC, Lee CJ, Liu KH, et al. All-inorganic perovskite quantum dot light-emitting memories. *Nat Commun* 2021;12:4460. DOI PubMed PMC
35. Gomez CM, Pan S, Braga HM, et al. Possible charge-transfer-induced conductivity enhancement in $TiO_2$ microtubes decorated with perovskite $CsPbBr_3$ nanocrystals. *Langmuir* 2020;36:5408-16. DOI PubMed
36. Chen C, Fu Q, Guo P, et al. Ionic transport characteristics of large-size $CsPbBr_3$ single crystals. *Mater Res Express* 2019;6:115808. DOI
37. Pu X, Zhao D, Fu C, et al. Understanding and calibration of charge storage mechanism in cyclic voltammetry curves. *Angew Chem Int Ed* 2021;60:21310-8. DOI PubMed
38. Jiang Q, Chen M, Li J, et al. Electrochemical doping of halide perovskites with ion intercalation. *ACS Nano* 2017;11:1073-9. DOI PubMed
39. Hwang JH, Islam MA, Choi H, et al. Improving electrochemical $Pb^{2+}$ detection using a vertically aligned 2D $MoS_2$ nanofilm. *Anal Chem* 2019;91:11770-7. DOI PubMed
40. Zhang X, Lin S, Chen Z, Megharaj M, Naidu R. Kaolinite-supported nanoscale zero-valent iron for removal of $Pb^{2+}$ from aqueous solution: reactivity, characterization and mechanism. *Water Res* 2011;45:3481-8. DOI PubMed
41. Pala IR, Brock SL. ZnS nanoparticle gels for remediation of $Pb^{2+}$ and $Hg^{2+}$ polluted water. *ACS Appl Mater Interfaces* 2012;4:2160-7. DOI PubMed
42. Woo YW, Jung Y, Kim GY, Kim S, Walsh A. Factors influencing halide vacancy transport in perovskite solar cells. *Discov Mater* 2022;2:8. DOI
43. Nur'aini A, Lee S, Oh I. Ion migration in metal halide perovskites. *J Electrochem Sci Technol* 2022;13:71-7. DOI
44. Li N, Jia Y, Guo Y, Zhao N. Ion migration in perovskite light-emitting diodes: mechanism, characterizations, and material and device engineering. *Adv Mater* 2022;34:e2108102. DOI PubMed
45. Cai J, Zhao T, Chen M, et al. Ion migration in the all-inorganic perovskite $CsPbBr_3$ and its impacts on photodetection. *J Phys Chem C* 2022;126:10007-13. DOI
46. Hussain T, Fatima K, Anjum A, et al. Experimental evidence of ion migration in aged inorganic perovskite solar cells using non-destructive RBS depth profiling. *Mater Adv* 2022;3:7846-53. DOI
47. Bella F, Renzi P, Cavallo C, Gerbaldi C. Caesium for perovskite solar cells: an overview. *Chem A Eur J* 2018;24:12183-205. DOI PubMed